Review of Scientific Instruments

Quantitative temperature distribution measurements by non-contact scanning thermal microscopy using Wollaston probes under ambient conditions

Cite as: Rev. Sci. Instrum. **91**, 014901 (2020); https://doi.org/10.1063/1.5099981
Submitted: 13 April 2019 . Accepted: 10 December 2019 . Published Online: 06 January 2020

Yun Zhang, Wenkai Zhu, Liang Han, and Theodorian Borca-Tasciuc

ARTICLES YOU MAY BE INTERESTED IN

AIP Publishing

Quantitative temperature distribution measurements by non-contact scanning thermal microscopy using Wollaston probes under ambient conditions

Cite as: Rev. Sci. Instrum. 91, 014901 (2020); doi: 10.1063/1.5099981
Submitted: 13 April 2019 • Accepted: 10 December 2019 •
Published Online: 6 January 2020

View Online Export Citation CrossMark

Yun Zhang, Wenkai Zhu, Liang Han, and Theodorian Borca-Tasciuc[a)]

AFFILIATIONS

Mechanical, Aerospace, and Nuclear Engineering Department, Rensselaer Polytechnic Institute, Troy, New York 12180, USA

[a)] **Author to whom correspondence should be addressed:** borcat@rpi.edu

ABSTRACT

Temperature measurement using Scanning Thermal Microscopy (SThM) usually involves heat transfer across the mechanical contact and liquid meniscus between the thermometer probe and the sample. Variations in contact conditions due to capillary effects at sample-probe contact and wear and tear of the probe and sample interfere with the accurate determination of the sample surface temperature. This paper presents a method for quantitative temperature sensing using SThM in noncontact mode. In this technique, the thermal probe is scanned above the sample at a distance comparable with the mean free path of ambient gas molecules. A Three-Dimensional Finite Element Model (3DFEM) that includes the details of the heat transfer between the sample and the probe in the diffusive and transition heat conduction regimes was found to accurately simulate the temperature profiles measured using a Wollaston thermal probe setup. In order to simplify the data reduction for the local sample temperature, analytical models were developed for noncontact measurements using Wollaston probes. Two calibration strategies (active calibration and passive calibration) for the sample-probe thermal exchange parameters are presented. Both calibration methods use sample-probe thermal exchange resistance correlations developed using the 3DFEM to accurately capture effects due to sample-probe gap geometry and the thermal exchange radii in the diffusive and transition regimes. The analytical data reduction methods were validated by experiments and 3DFEM simulations using microscale heaters deposited on glass and on dielectric films on silicon substrates. Experimental and predicted temperature profiles were independent of the probe-sample clearance in the range of 100–200 nm, where the sample-probe thermal exchange resistance is practically constant. The difference between the SThM determined and actual average microheater temperature rise was between 0.1% and 0.5% when using active calibration on samples with known thermal properties and between ~1.6% and 3.5% when using passive calibration, which yields robust sample-probe thermal exchange parameters that can be used also on samples with unknown thermal properties.

I. INTRODUCTION

Local temperature determination is one of the critical needs for thermal management of miniaturized electronic devices.[1] Scanning thermal microscopy (SThM) techniques employ probes with superior spatial resolution when compared to micro-Raman thermometry,[2,3] optical thermometry,[4,5] and infrared thermal microscopy.[6,7] SThM is based on Atomic Force Microscopy (AFM) with a special tip functioning as a temperature sensor and/or heat source, which helps to measure local sample temperature or thermal properties[8] and can scan with nanoscale spatial resolution.[9] SThM can operate in active or passive modes depending on whether the probe is self-heated or not. Noncontact mode indicates the absence of mechanical contact due to nonzero tip-sample clearance and has been reported for sample thermal conductivity measurements.[10–12] To quantitatively measure sample temperature by SThM, various methods including double scan,[13] null-point method,[14–17] and two scan method[18–20] were developed and are briefly discussed below.

The double scan technique[13] used the difference between SThM thermocouple probe temperatures collected in contact and noncontact mode in order to eliminate the influence of air conduction on the temperature measurement. The null-point method[14–17] implemented double scan procedures for thermocouple probes instrumented with heaters to induce low to high probe temperatures and to interpolate a point where the heat exchange between the probe and the sample was equal to zero, signifying that the temperature of the probe and sample were equal. The two scan method[19] was developed for a resistive thermal probe operating in vacuum conditions and considered the variations with the sample location of the thermal contact resistance, which is the thermal resistance between the tip region of the probe that comes in contact with the sample and the sample surface. This method measured the thermal contact resistance when the sample heating was turned on and off. The temperature rise of the sample for the heating on state was assumed to be small enough compared to the temperature rise of the probe, and thus, thermal contact resistance remained constant for the heating on and heating off states. An analytical model was used to determine the local sample temperature while considering a position dependent tip-sample thermal resistance.

The SThM based sample temperature sensing methods discussed above involve measurements done in mechanical contact between the probe and sample. However, tip-sample contact thermal resistance does vary with the topography of the sample[18,21] and with wear and tear of the probe/sample contact region due to mechanical contact changes or when the temperature rise of the sample becomes significant.[22,23] This requires additional modeling or related experimental characterizations to more accurately determine the tip-sample thermal resistance and its variation.[24–29] In addition to the solid-solid contact, the liquid meniscus between the probe and sample plays a major role in the heat transfer at the tip-sample contact. That could also affect the temperature measurement accuracy in contact mode.[24] While SThM under ultrahigh vacuum could eliminate the heat conduction through the water meniscus, control of the heat transfer through the mechanical contact remains a challenge.[30] Moreover, near-field thermal radiation transfer across the contact region could become a dominant heat transfer mechanism,[31] but it is not thoroughly understood.[24]

This paper presents a method for quantitative temperature sensing using scanning thermal microscopy in noncontact mode under ambient conditions, which eliminates uncertainties due to liquid meniscus and wear, tear, and control of the solid-solid contact. In this noncontact technique,[11,32] the thermal probe is scanned above the sample at a distance comparable with the mean free path of ambient gas molecules. A Three-Dimensional Finite Element Model (3DFEM) that includes the details of the heat transfer between the sample and the probe in diffusive and transition heat conduction regimes was developed and was found to accurately simulate the temperatures measured using a Wollaston thermal probe setup. In order to simplify the data reduction procedure for the local sample temperature, analytical models were employed for noncontact measurements using Wollaston probes. Two calibration strategies are presented (active calibration and passive calibration) for the sample-probe thermal exchange parameters required by the analytical models. Both calibration methods use one set of experiments in conjunction with a newly developed sample-probe thermal exchange resistance correlation. This correlation was developed for Wollaston probes using the 3DFEM and accurately captures effects due to sample-probe gap geometry and the thermal exchange radii in both the diffusive and transition regimes. The analytical data reduction methods were validated by experiments and 3DFEM simulations using metallic microscale heaters patterned on glass and silicon substrates.

II. EXPERIMENTAL SETUP

A. Experimental setup

The samples used for the SThM temperature measurement experiments are gold microheaters/thermistors of 10–40 μm widths, microfabricated in a cleanroom on glass and silicon substrates. As all the aforementioned work[13–20] used the line heater to validate their techniques, the microheater samples with similar geometry are used in the following experiments and are shown on the left side of Fig. 1. A DC power supply is connected to the inner pair of the electrical pads of the microheater and provides a constant current through the microheater region shown in red in Fig. 1. The Joule heating yields a temperature profile in the sample confined near the heater. In a typical SThM temperature measurement experiment, the SThM probe is scanned above the middle section of the microheater along a direction perpendicular to its length, as shown. To experimentally validate the SThM sample temperature measurements performed in this work, the outer pair of the electrical pads is connected to a data acquisition system to measure the voltage across the middle section of the microheater in order to determine its temperature rise from its temperature coefficient of resistance (TCR_s) and electrical resistance change.

Figure 1 shows on the right the schematic of the automatic noncontact SThM temperature sensing system. The sample is mounted on an XYZ nanopositioning system which enables three-dimensional scanning. A laser beam reflected by a small mirror on the probe cantilever is detected by a photodiode detector. The probe is a commercial Veeco® Wollaston thermal probe consisting of a Pt/Rh core of 5-μm diameter and a 75-μm diameter silver shell. In

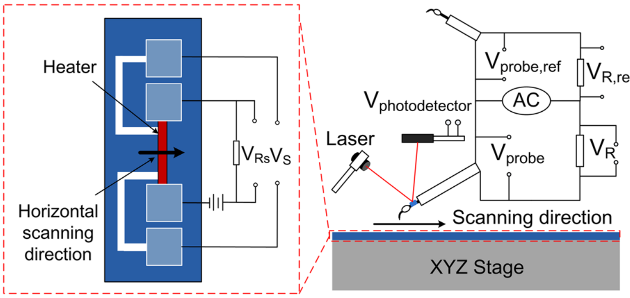

FIG. 1. Left: Top view of a microheater. Right: Schematic of the noncontact temperature scanning system. V_s, V_{Rs}, $V_{photodetector}$, V_{probe}, and V_R are the voltage signals across the microheater, the series resistor of microheater circuit, the photodetector, the thermal probe, and the series resistor of the thermal probe, respectively. Another parallel circuit consisting of a reference probe and a series resistor is used to monitor changes in the heat transfer of the probe with the laboratory ambient, where $V_{probe,ref}$ and $V_{R,ref}$ are voltage signal across the reference probe and reference series resistor, respectively.

the active mode, an AC current with a frequency of 6 kHz and a current range of 10–19 mA is applied to the probe, while the microheater is not energized. In the passive mode, the microheater is energized, while a smaller AC current range of 0.1–1 mA is applied through the probe to minimize self-heating effects during the probe temperature measurement experiments. A parallel circuit consisting of a reference probe and a series resistor is used to monitor changes in the heat transfer of the probe with the laboratory ambient. A data acquisition system collects simultaneously voltage signals from the SThM probe setup and the microheater setup.

B. Probe average temperature measurement

Figure 2 shows the electrical resistance of a Wollaston SThM probe measured as a function of the square of the probe current, for a tip-sample clearance of 300 nm on top of a 40 μm microheater on a glass substrate. The change in the probe electrical resistance indicates a change in the average temperature of the probe, which is affected by Joule heating due to the probe current and also by the sample surface temperature. For a fixed sample temperature, the electrical resistance changes linearly with the current squared, with the slope of the curve being proportional to the thermal resistance of the probe. The probe electrical resistance value for zero current is represented by the intersection of the curve with the y-axis and changes with the sample temperature, as shown by the set of curves collected for sample temperature rises between 0 K and 80 K above ambient. The no heating resistance R_{p0} when the sample is not heated and the probe has zero current can be located on the graph. Therefore, the average probe temperature rise T^*_{ave} can be calculated by Eq. (1) due to the proportionality of sample temperature rise and probe electrical resistance,

$$T^*_{ave} = \frac{R - R_{p0}}{R_{p0} \times TCR_p}, \tag{1}$$

where the $R_{p0} = 2.2665\ \Omega$, $TCR_p = 0.001\,65\ \mathrm{K}^{-1}$ [33] is the temperature coefficient of resistance of the probe, and R is the probe electrical resistance measured at every step of scanning, respectively.

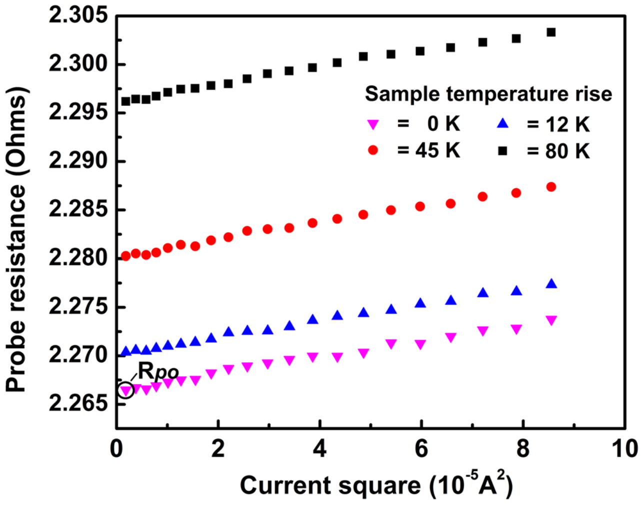

FIG. 2. SThM probe electrical resistance vs SThM probe current squared for different sample temperature rises, as measured at a tip-sample clearance of 300 nm.

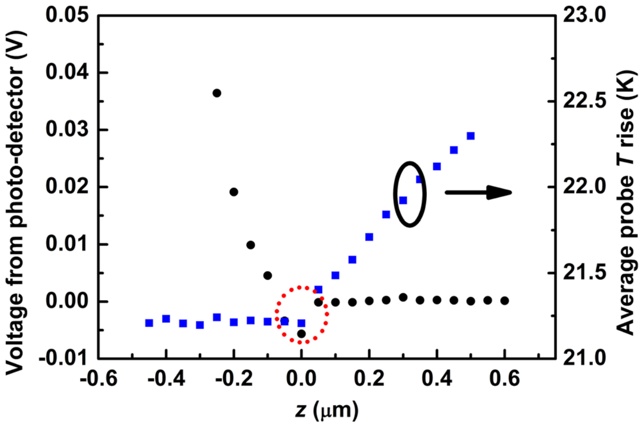

FIG. 3. The photodetector signal and the average temperature rise of the SThM probe during a vertical scanning in active mode with nonheated sample.

C. Scanning procedures

To locate the contact point and then set the tip-sample clearance, a vertical scanning with a 50-nm step size was performed first by gradually raising the sample. The contact point was determined for several locations on the sample using experimental data similar to the one shown in Fig. 3 collected using the probe in active mode. Before the sample-probe contact, the laser detector signal was constant, and heat transfer through air was the only heat transfer mechanism between the sample and the probe. The average probe temperature rise T^*_{ave} decreased linearly with the decreasing of the tip-sample distance. When the probe contacted the sample surface, there was a voltage change of the laser detector and a sudden temperature drop of the probe due to additional solid-solid and water meniscus heat conductions. After the contact, the signal from the laser sensor kept increasing linearly as the probe cantilever was deflected further, while the probe temperature rise reached a constant value with some small fluctuations. The probe temperature and the distance from the sample surface of each point were recorded, and the force feedback system was used to monitor the tip-sample clearance.

Horizontal scanning typically with 1–10 μm step size and at a constant tip-sample clearance was performed across the heater width as indicated in Fig. 1. The probe tip-sample clearance was set to values in the range of 100 nm–300 nm.

In order to obtain the temperature of the sample, analytical and finite element models for the heat transfer between the probe and the sample have been developed and are described in Secs. III and IV.

III. ANALYTICAL MODELING

A. Active mode

The active mode is typically employed for measuring the thermal conductivity of the sample.[30] In this work, it is used to help calibrate the thermal exchange parameters between the apex of the probe and the sample. The governing equation of the one-dimensional fin model for the Joule heated Wollaston probe was developed in Ref. 11, as shown at steady state in the following equation:

$$\frac{d^2T^*}{dx^2} - \left(\frac{2h_{\text{eff}}}{k_p r} - \frac{I^2\rho_0 TCR_p}{k_p\pi^2 r^4}\right)T^* + \frac{I^2\rho_0}{k_p\pi^2 r^4} = 0, \tag{2}$$

where for a point x on the probe, T^* represents the local temperature rise above the ambient temperature, ρ_0 and k_p are the probe's electrical resistivity and thermal conductivity at the ambient temperature, h_{eff} is the effective heat transfer coefficient, TCR_p is the probe's temperature coefficient of resistance, I is probe's current, and $r = d/2$ is the radius of the Wollaston wire probe. The schematic of this analytical model is shown in Fig. 4.

The general formula of the analytical solution of Eq. (2) is

$$T^* = C_1 e^{\lambda x} + C_2 e^{-\lambda x} + \frac{S}{\lambda^2}, \tag{3}$$

where

$$\lambda = \left(\frac{2h_{\text{eff}}}{k_p r} - \frac{I^2\rho_0 TCR_p}{k_p\pi^2 r^4}\right)^{0.5}, \tag{4}$$

$$S = \frac{I^2\rho_0}{k_p\pi^2 r^4}. \tag{5}$$

Assuming the silver clad and the probe cantilever are ideal heat sinks that yield no temperature rise at that probe ends,

$$T^*|_{x=0} = T^*|_{x=2L} = 0. \tag{6}$$

For the tip region of the probe, the heat transfer rate Q_s between the probe tip and sample surface can be found from the energy balance, which due to symmetry can be written as

$$-k_p A_p \frac{\partial T^*}{\partial x}\Big|_{x=L-b} + \frac{I^2\rho_0 b}{A_p}\left(1 + TCR_p \times T^*|_{x=L-b}\right) - h_{\text{eff}} b\pi r T^*|_{x=L-b} = \frac{Q_s}{2}, \tag{7}$$

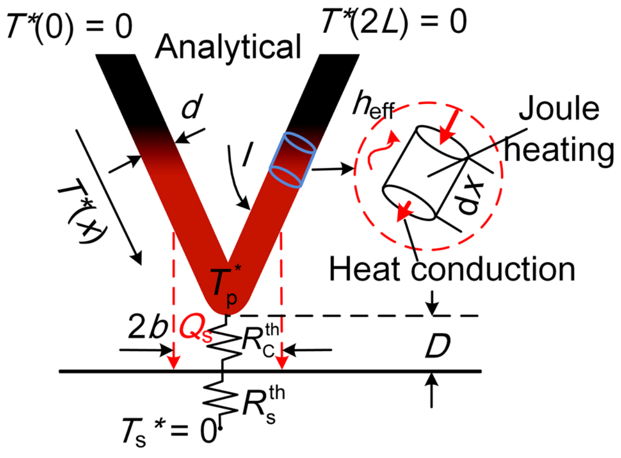

FIG. 4. Analytical model of the probe and probe tip heat transfer.

where A_p is the cross-sectional area of the probe. In Eq. (7), h_{eff} acts on the upper surface of the 2b tip region shown in Fig. 4, while the bottom tip region exchanges heat directly with the sample surface.

Then, the heat transfer rate in the sample can be written as

$$Q_s = \frac{T^*|_{x=L-b}}{R_S^{th} + R_C^{th}}, \tag{8}$$

where R_C^{th} is the tip-sample thermal exchange resistance and L is the half-length of the probe. The temperature rise for the tip region is $T_p{}^* = T^*|_{x=L-b}$. Assuming that the tip-sample heat transfer rate Q_s occurs through a disk-shaped area with radius b of uniform temperature distribution on the sample surface, the thermal resistance for a bulk sample is expressed by

$$R_S^{th} = \frac{1}{4k_s b}, \tag{9}$$

where k_s is the thermal conductivity of the sample.

Finally, the averaged probe temperature can be calculated from

$$T^*_{\text{ave}} = \frac{1}{L}\int_0^L T^* dx. \tag{10}$$

B. Passive mode

For temperature sensing applications, the SThM probe runs in the passive mode. The Joule heating effect for the probe under a small current is neglected, and Eq. (2) can be simplified to

$$\frac{d^2T^*}{dx^2} - \frac{2h_{\text{eff}}}{k_p r}T^* = 0. \tag{11}$$

The boundary conditions [Eqs. (6) and (7)] become

$$T^*|_{x=0} = T^*|_{x=2L} = 0, \tag{12}$$

$$-k_p A_p \frac{\partial T^*}{\partial x}\Big|_{x=L-b} - h_{\text{eff}} b\pi r T^*\Big|_{x=L-b} = \frac{Q_s}{2}. \tag{13}$$

The analytical solution of Eq. (11) is written as a function of Q_s,

$$T^*(x) = Q_s\left(C_1 e^{\sqrt{A}x} + C_2 e^{-\sqrt{A}x}\right), \tag{14}$$

where

$$C_1 = -\left[b h_{\text{eff}}\pi r \sinh\left(\sqrt{A}(L-b)\right) + \sqrt{A}A_p k_p \cosh\left(\sqrt{A}(L-b)\right)\right]^{-1}, \tag{15}$$

$$C_2 = -C_1, \tag{16}$$

$$A = \frac{2h_{\text{eff}}}{k_p r}. \tag{17}$$

Then, the average temperature rise of the probe T^*_{ave} can be calculated by averaging $T^*(x)$ over the length of the probe, as shown in Eq. (10).

Next, the sample temperature rise can be calculated as

$$T_s^* = T_p^* + R_C^{th} \times Q_s, \tag{18}$$

where T_p^* and T_s^* are the temperature rise of the probe tip and sample, respectively. Two parameters R_C^{th} and b are required by the analytical models described in this section in order to obtain numerical results. The calibration of these parameters is discussed in Sec. V.

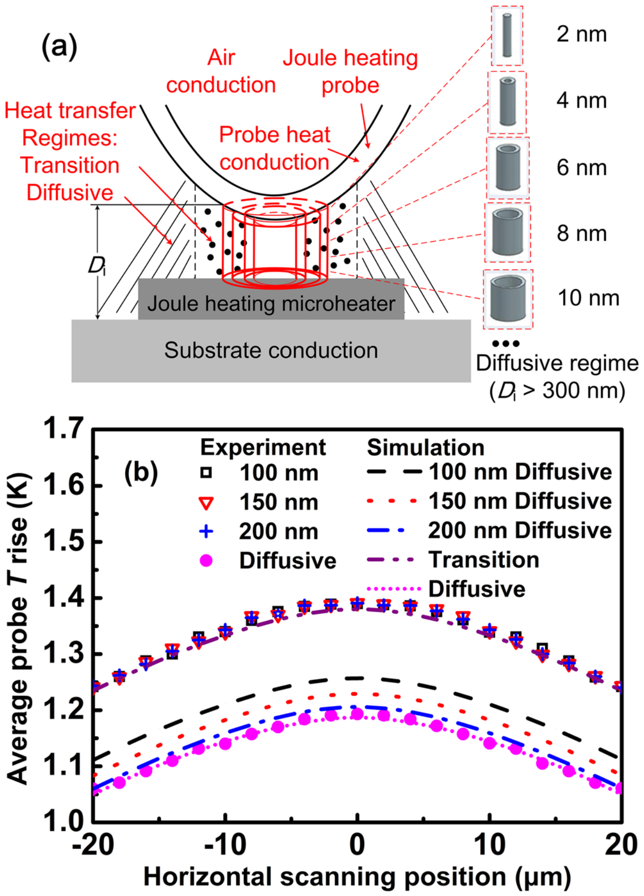

FIG. 5. (a) 3DFEM modeling of the sample-probe-ambient heat transfer. The tip-sample air gap was decomposed into tubes with identical wall thickness which were assigned thermal conductivity values based on the local tip-sample clearance according to Eq. (23) for the transition regime; (b) Comparison between experimental and 3DFEM predictions of the average probe temperature rise measured across a 40-μm microheater on glass substrate and with apex probe-sample clearances in the transition (100–200 nm) and diffusive (300 nm) heat transfer regimes.

IV. 3DFEM FOR SAMPLE-PROBE-AMBIENT HEAT TRANSFER

A. FEM model

A 3-Dimensional Finite Element Model (3DFEM) was implemented in COMSOL Multiphysics®[34] to simulate the heat transfer between the probe, the sample, and the surrounding air. The geometrical model of the SThM probe and sample used by the 3DFEM simulations are shown in Fig. 5(a) and are similar to those used in experiments. Probe and modeling parameters used by 3DFEM and analytical models are listed in Table I. The computational domain consists of four parts: the probe, the sample, the air gap between the probe and the sample, and the surrounding air. The heat transfer mechanism between the probe and air was shown to be heat conduction for the Wollaston probe geometry.[10,11] Two key physical processes are involved, one is Joule heating in the thermal probe and the other is heat conduction among the computational domains. Therefore, the energy equation in each part of the computational domain can be expressed as

$$-\nabla\cdot(k\nabla T) = Q, \tag{19}$$

where Q is the volumetric heat source, and k is the thermal conductivity of each part of the domain. The bulk thermal conductivity of the microheaters' glass substrate, probe, and air are 1.1, 38, and 0.026 W m^{-1} K^{-1},[35,36] respectively.

In the passive mode, a volumetric heat source Q is applied to the metallic heater sample and set to be zero in other domains.

In active mode, the probe has Q according to Eq. (20), and Q in other domains is set to be zero,

$$Q = J\cdot\mathbf{E}, \tag{20}$$

where

$$J = \sigma\mathbf{E}, \tag{21}$$

$$\sigma = \frac{1}{\rho_0\left(1 + TCR_\mathrm{p}(T - T_\mathrm{ref})\right)}, \tag{22}$$

where E is electric field strength (V m^{-1}), J is the current density (A m^{-2}), and σ is the electrical conductivity (S m^{-1}), respectively.

TABLE I. Probe and 3DFEM and analytical modeling parameters.

Attribute	Symbol	Unit	Value in model
Probe half length	L	μm	100
Probe radius	r	μm	2.5
Probe tip radius of curvature	R_curve	μm	12
Probe half-angle	Θ	deg	18
Thermal conductivity of probe	k_p	W m^{-1} K^{-1}	38
Probe electrical resistivity (19.9 °C)	ρ_0	Ω m	2.06×10^{-7}
Temperature coefficient of resistance	TCR_p	K^{-1}	0.001 65
Thermal conductivity of air in free space	k_0	W m^{-1} K^{-1}	0.026 2[10]
Effective heat transfer coefficient	h_eff	W m^{-2} K^{-1}	1 700
Tip-sample clearance at tip apex	D	nm	Varies (50–300)
Heat generation of 40-μm microheater on glass substrate	P	W	0.016

Since the tip-sample clearance (100–300 nm) is comparable to the mean free path of ambient air, the interactions between gas molecules and boundaries become more pronounced, which reduces the gas thermal conductivity compared to its bulk value. According to Refs. 37–39, the thermal conductivity of an air layer in the transition regime can be estimated by

$$k_f = \frac{k_0}{1 + 2\frac{2-\sigma_T}{\sigma_T}\frac{2\gamma}{\gamma+1}\frac{\lambda/D_i}{\mathrm{Pr}}}, \tag{23}$$

where λ and k_0 are the mean free path and the thermal conductivity of air in free space. σ_T is the thermal accommodation coefficient ($\sigma_T = 1$[38]), γ is the ratio of the specific heats, Pr denotes the Prandtl number, and D_i is the local clearance from sample to probe. The ratio λ/D_i is equivalent to the Knudsen number (Kn). The 3DFEM of the air gap between the probe and the sample in the transition regime was forced to account for Eq. (23) by decomposing the gap in an array of coaxial tube sections with constant wall thickness starting from the apex of the probe. The decomposition process is shown in Fig. 5(a). Each tube was set to the corresponding effective thermal conductivity from Eq. (23), based on the tube's height, which is the local tip-sample clearance D_i. If the local clearance is ≥300 nm, the decomposition process is stopped and the air thermal conductivity assumes the bulk value.

The initial value of the temperature was set to $T_{\mathrm{ref}} = 299.05$ K for all the computational domain as well as the external boundaries of the air box (far from the thermal probe). Solution convergence studies were conducted with 587 414, 634 234, 745 386, 941 173, and 1 055 557 triangular meshes, respectively. Since the difference of computation results (temperature) from 745 386 meshes to 1 055 557 meshes was only in the order of 1×10^{-6}, 941 173 meshes were chosen.

B. 3DFEM validation for noncontact SThM with air-gap heat transfer in the transition and the diffusive regimes

Figure 5(b) shows a comparison between 3DFEM predictions for T^*_{ave} profiles and experimental results for a Wollaston SThM probe scanned in passive mode at tip-sample clearances of 100 nm, 150 nm, 200 nm, and 300 nm above a 40-μm width microheater deposited on a glass substrate. The difference between the average heater temperature rise calculated from the TCR_s of microheater and the 3DFEM simulation was under 0.12% when inputting the same power from the experiments to the microheater model. The experimental uncertainty for the thermistor based measurement of the average heater temperature is 0.07%. The experimental uncertainties for T^*_{ave} profiles reported in Fig. 5(b) are <0.34%, the corresponding error bars being smaller than the size of the experimental dots. The 3DFEM simulations of T^*_{ave} are in good agreement with the experiments for both the diffusive and transition heat transfer regimes of heat conduction in the tip-sample air gap. Moreover, T^*_{ave} profiles for probe tip-sample clearances of 100 nm, 150 nm, and 200 nm were observed to overlap in both experiments and the 3DFEM simulations performed in the transition regime. However, 3DFEM simulations that employ the bulk thermal conductivity of the air in the entire domain do not yield good agreement with experiments, unless the gaps are 300 nm or larger. This indicates that the implementation of transition regime heat conduction was critical to predict accurately the temperature profiles measured by the SThM probe for gaps <200 nm.

C. Development of sample-probe thermal exchange resistance correlation

An analytical model, a correlation, or experimental values for the sample-probe thermal exchange resistance $R^{\mathrm{th}}_{\mathrm{C}}$ are needed for implementing the analytical models developed in Sec. III in order to determine the sample surface temperature from the measured probe temperature. While the sample-probe thermal exchange resistance was measured experimentally in both diffusive and transition regimes,[10,11,40] there are few references that considered analytical models for conduction in the air gap.[24] Majumdar *et al.*[8] introduced a model to estimate thermal exchange resistance by taking tip-sample clearance as the new MFP in the kinetic theory for the transitional regime. Analytical $R^{\mathrm{th}}_{\mathrm{C}}$ models that account for both diffusive and transition regime for a spherical probe are presented in Refs. 40 and 41. However, these models do not describe Wollaston probe heat transfer accurately when the heat transfer radius is comparable with the wire diameter. Gomes *et al.*[24] further suggested to use simulations to study thermal interaction in the transition regime.

This work employs 3DFEM for the apex section of the probe in order to develop a correlation for $R^{\mathrm{th}}_{\mathrm{C}}$ of a Wollaston probe apex geometry. The correlation accounts for the tip-sample clearance D, the heat transfer radius b, and the probe wire diameter d. As shown in Fig. 6, the region between the sample surface and the apex of the probe was cut into cylindrical sections with diameters $2b$ ranging from 1 μm to 10 μm, representing different diameters of the heat transfer regions between the probe and the sample. The rest of the system was removed from this simulation. A gap-dependent air thermal conductivity calculated using Eq. (23) was assigned to cylindrical subsections within the $2b$ region using the process already discussed in Sec. IV B and shown in Fig. 5(a). For a given $2b$ region, the lateral and top surfaces were set to be adiabatic. The sample portion included in this region (the bottom surface) was fixed at the room temperature, while the probe segment included in this region was heated until its steady state temperature reached 310 K. The required power was recorded and $R^{\mathrm{th}}_{\mathrm{C}}$ was calculated using Eq. (18).

Figure 7(a) shows examples of $R^{\mathrm{th}}_{\mathrm{C}}$ calculated as a function of b for a probe of $d = 5$ μm diameter set in either the diffusive ($D = 300$ nm) or transition regime ($D = 100$ nm). Examples of simulation results for $R^{\mathrm{th}}_{\mathrm{C}}$ as a function of tip-sample clearance with $d = 5$ μm and $b = 2$ μm are shown in Fig. 7(b). In the transition regime, the modeled $R^{\mathrm{th}}_{\mathrm{C}}$ is found to be nearly independent of the tip-sample clearance D. This result explains the clearance independent experimental probe temperature profiles from Fig. 5(b) obtained for 100–200 nm probe-sample clearances. On the contrary, for Kn < 0.01, $R^{\mathrm{th}}_{\mathrm{C}}$ varies significantly with D in the diffusive regime. Figure 7(c) shows simulation results for $R^{\mathrm{th}}_{\mathrm{C}}$ with $b = 1$ μm as a function of probe diameter in the diffusive ($D = 300$ nm) and transition ($D = 100$ nm) regimes.

Correlations were developed by fitting the 3DFEM simulation results for $R^{\mathrm{th}}_{\mathrm{C}}$ (in Kelvin per Watts) using D (in nanometer), b (in

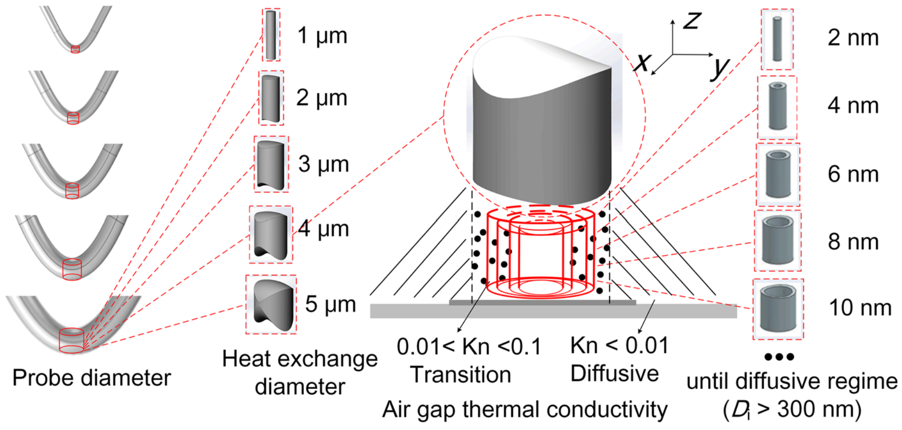

FIG. 6. Left: Schematic of probes with different diameters. Cylindrical sections of the probe and air gap (displayed upside down) depict heat transfer regions with different diameters for each probe. The right side of the image depicts the decomposition of the air gap for a given probe and heat transfer diameter in cylinders with thermal conductivities based on the local gap clearance and Eq. (23).

micrometer), and d (in micrometer) as variables and yielding

$$R_C^{th} = 1.871\,11 b^{-0.278\,83} d^{-0.007\,02} (114\,602.3 - 178.698D + 0.801\,08D^2)$$
$$0 < D < 300 \text{ nm},$$

$$R_C^{th} = 3.2037 b^{-0.149\,35} d^{-0.050\,65} (141\,248.8 - 618.202D + 1.359\,61D^2)$$
$$300 \text{ nm} \leq D \leq 350 \text{ nm}. \qquad (24)$$

The correlation fits very well the 3DFEM numerical solutions, as shown in Fig. 7. The correlation coefficient for the fit was $R^2 = 0.9915$.

V. EXPERIMENTAL RESULTS AND DISCUSSION

A. Calibration of heat exchange parameters

The analytical model described in Sec. III B can be used to determine the sample temperature based on the measured average probe temperature; however, it needs the calibrated values for the thermal exchange parameters R_C^{th} and b. The strategy described in this work for determining b and R_C^{th} requires one experimental calibration and the use of the sample-probe thermal exchange resistance correlation developed in Sec. IV C. The experimental calibration can be performed in the active and passive operation modes as described below.

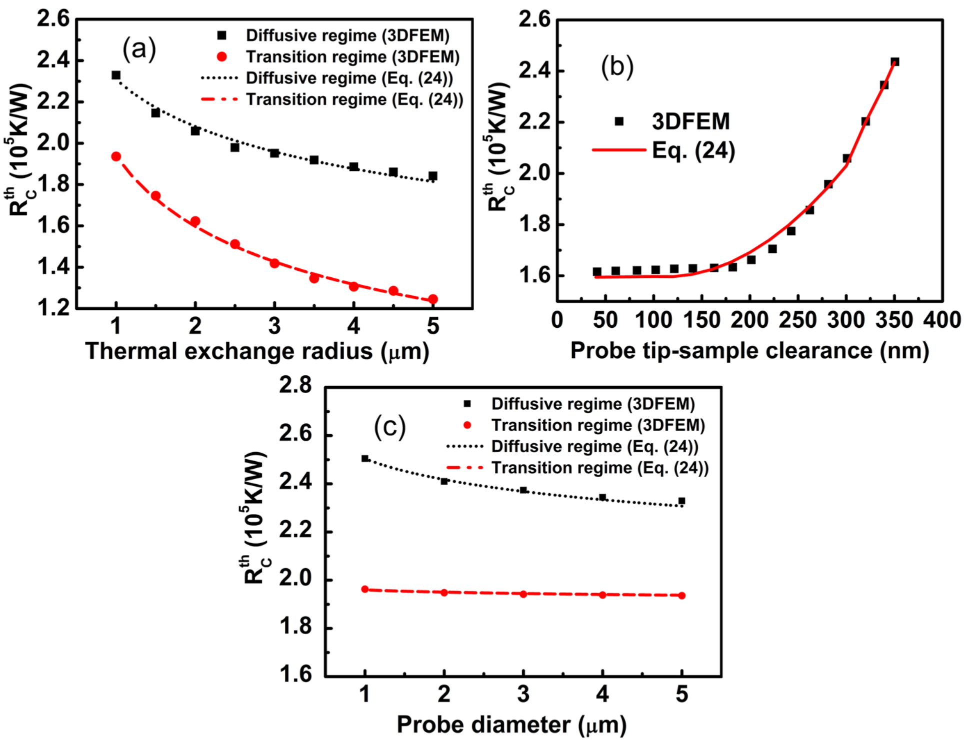

FIG. 7. (a) 3DFEM results (dots) compared with predictions of the developed correlation Eq. (24) for R_C^{th} as a function of: (a) heat transfer radius b for $d = 5$ μm in the diffusive ($D = 300$ nm) and the transition regime ($D = 100$ nm), (b) D with $b = 2$ μm and $d = 5$ μm, and (c) d with heat transfer radius $b = 1$ μm in the diffusive ($D = 300$ nm) and the transition ($D = 100$ nm) regime.

In the active mode, the thermal resistance of the probe is measured above a bulk sample of known thermal conductivity. Similar to the procedure described in Ref. 11, for each heat transfer radius b selected in a range between 0.5 and 5 μm, the analytical model described in Sec. III A is used to fit the average probe temperature rise T_{ave}^* to its experimentally measured value and determine R_C^{th} from the relationship

$$R_c^{th} = \frac{T_p^*}{Q_s} - R_s^{th}. \tag{25}$$

In the passive mode the SThM probe is scanned across the width of a microheater of known average temperature. The values of the averaged SThM probe temperature measured at several points across the width of the microheater line in the center of the microheater are averaged yielding an averaged SThM profile temperature.

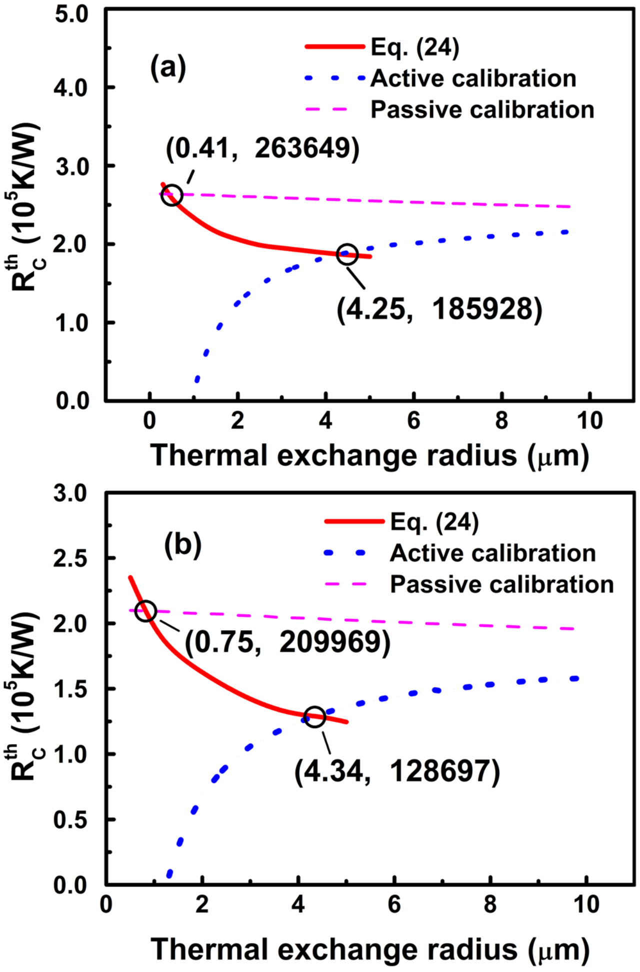

FIG. 8. Finding the values of the thermal exchange parameters R_C^{th} and b using active and passive mode calibrations in (a) diffusive regime with D = 300 nm and (b) transition regime with D = 100 nm. The intersections of the experimental calibration curves with the thermal exchange resistance correlation [Eq. (24)] yield the results specified in each figure.

Then, for a heat transfer radius b selected in a range between 0.5 and 5 μm the analytical model described in Sec. III B is used to fit T_{ave}^* to the averaged SThM profile temperature and determine R_C^{th} from the relationship

$$R_C^{th} = (T_s^* - T_p^*)/Q_s. \tag{26}$$

Figure 8 shows with blue dot lines the active mode experimental calibration curves collected for tip-sample clearances in the diffusive [Fig. 8(a)] and transition [Fig. 8(b)] heat transfer regimes using a glass substrate with known thermal conductivity

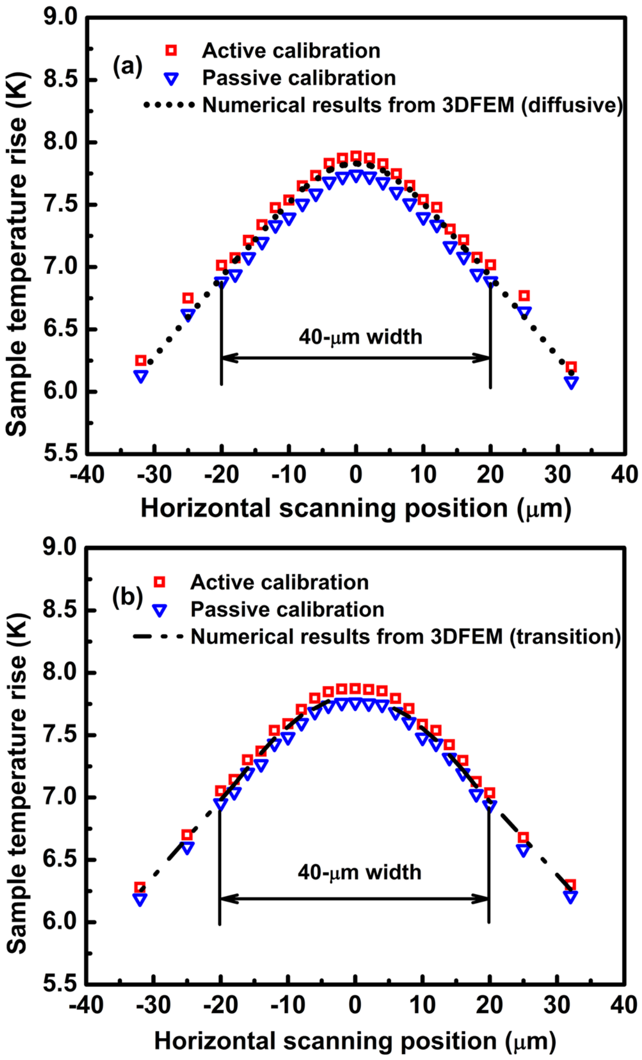

FIG. 9. Comparison between SThM experimental results (dots) and predictions (lines) of the temperature rise profiles around a 40-μm microheater deposited on a glass substrate and for scanning tip-sample clearances of (a) 300 nm and (b) 100 nm. The experimental data reduction employed thermal exchange parameters calibrated in either active mode (squares) or passive mode (triangle) regimes. The physical extent of the metallic heater is indicated in each figure. The uncertainties of sample temperature rises were primarily from measured average probe temperature with a maximum of 0.04 K.

($k_s = 1.1$ W m^{-1} K^{-1}). Similarly, the passive mode experimental calibration curves for each heat transfer regime are shown with pink dash lines. The passive mode sample was a 40 μm microheater on a glass substrate with an average temperature rise of 8.1 K. The final step in the calibration procedure is to intersect the experimental calibration curves with the curves described by Eq. (24). This process is shown graphically in Figs. 8(a) and 8(b), where the sample-probe thermal exchange resistance correlation is shown with red line.

The solutions for R_C^{th} and b resulting from these intersections are used to obtain the sample temperature rise when employing the analytical models from Sec. III B. The active mode and passive mode calibration procedures yield significantly different solutions for the probe-sample thermal exchange parameters, with the passive calibration yielding consistently smaller b and higher R_C^{th} than active mode calibration. Kim's group suggested a correlation between the thermal contact radius and spatial resolution,[26] and therefore, the ~0.7 μm thermal exchange radius is referred to as the spatial resolution of the passive mode temperature sensing experiment.

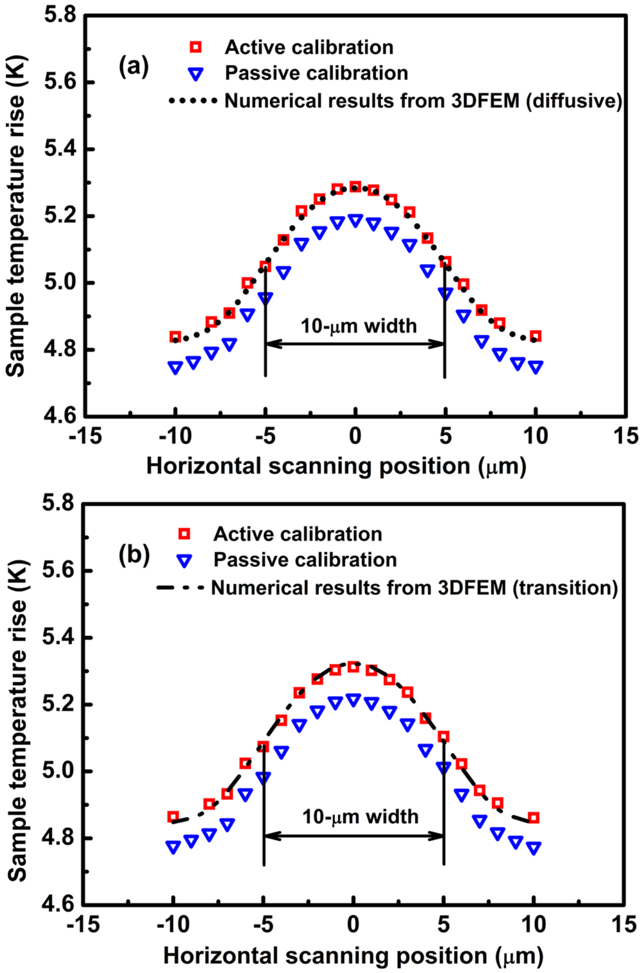

FIG. 10. Comparison between SThM experimental results (dots) and predictions (lines) of the temperature rise profiles around a 10-μm microheater deposited on a glass substrate and for scanning tip-sample clearances of (a) 300 nm and (b) 100 nm. The experimental data reduction employed thermal exchange parameters calibrated in either active mode (squares) or passive mode (triangle) regimes. The physical extent of the metallic heater is indicated in each figure. The uncertainties of sample temperature rises were primarily from measured average probe temperature with a maximum of 0.02 K.

The effects of the calibration method on the measured sample temperature are discussed in Sec. V B.

B. Experimental results for SThM based noncontact temperature measurements

Figure 9 shows the comparison between 3DFEM simulated and experimentally determined microheater temperature rise profiles around a 40-μm microheater deposited on a glass substrate. The experimental profiles are determined from the measured average SThM probe temperature rise shown in Fig. 5(b), by using the passive mode analytical model developed in Sec. III B and sample-probe thermal exchange parameters from both active and passive mode calibration methods shown in Fig. 8. Results are shown for tip-sample clearances of 300 nm (diffusive regime) in Fig. 9(a) and 100 nm (transition regime) in Fig. 9(b). Using the active calibration thermal exchange parameters in the data reduction provided results closer to the 3DFEM simulations, with a maximum difference from the predicted heater temperature rise profiles of 1.09% for experiments performed at 300 nm tip-sample clearance and 0.81% for the 100 nm tip-sample clearance. The passive calibration method yielded a slightly higher maximum difference of 0.86% and 1.54% for the 100 nm and 300 nm tip-sample clearances, respectively. The results using passive calibration parameters are consistently below the predicted temperature rise, while the results using the active calibration parameters are consistently above predictions.

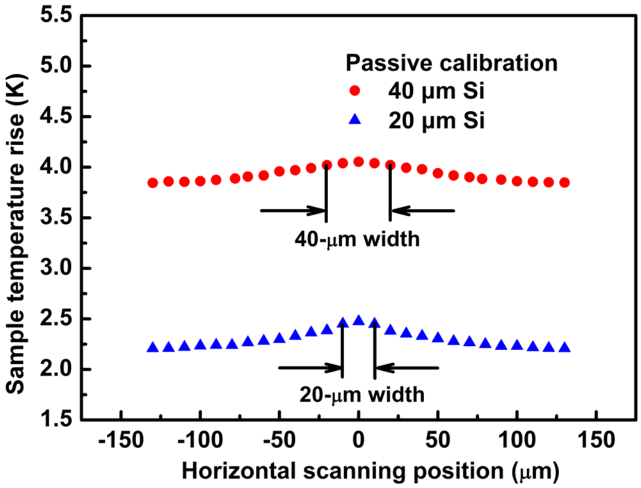

FIG. 11. Experimental temperature rise profiles measured around 40-μm and 20-μm microheaters deposited on a dielectric film on silicon substrate and measured by SThM at a 300 nm tip-sample clearance. The SThM temperature rise averaged over the physical extent of each heater (as indicated) is in agreement (between 2.9% and 3.5%) with the thermistor based average heater temperature rise reported in Table II. The uncertainties of sample temperature rises were primarily from measured average probe temperature with a maximum of 0.04 K.

TABLE II. Comparison between thermistor measured average heater temperature rise and SThM experiments using active and passive calibration methods and tip-sample clearances in the diffusive and transition regimes.

Experimental average temperature rise (K) from TCR_s	40 μm–glass 7.57		10 μm–glass 5.22		40 μm–Silicon 4.16	20 μm–Silicon 2.56
	Diffusive	Transition	Diffusive	Transition	Diffusive	Diffusive
Active calibration	7.53	7.58	5.21	5.24	3.46	2.11
Discrepancy (%)	0.5	0.1	0.2	0.4	16.8	17.6
Passive calibration	7.38	7.45	5.07	5.08	4.04	2.47
Discrepancy (%)	2.5	1.6	2.9	2.7	2.9	3.5

In order to investigate the accuracy of the temperature profile determination using the SThM technique when the size of the heater is reduced, the experiments and analysis procedures were repeated for a 10 μm width microheater deposited on glass substrate. The experimental temperature rise profile around the microheater was determined by employing the same analytical model developed in Sec. III B and the same active and passive mode probe-sample thermal exchange parameters determined from Fig. 8. The comparison between experimental results based on the two calibration methods and the sample temperature rise profile simulated by 3DFEM is shown in Fig. 10 for tip-sample scan clearances of 300 nm [Fig. 10(a)] and 100 nm [Fig. 10(b)]. The active calibration thermal exchange parameters yielded a more accurate experimental determination of the temperature profile as compared with using the passive mode calibration results. The maximum deviation from the predicted heater temperature rise profiles is 0.82% for experiments performed at 300 nm tip-sample clearance and 0.85% for the 100 nm tip-sample clearance, which are close to the temperature measurement accuracies obtained on the wider heater. The passive calibration method had a slightly higher deviation of 2.19%–2.69% for the 100 nm and 300 nm tip-sample clearances, respectively. Nevertheless, both calibration methods provided a good accuracy for the temperature profile measurements for both microheater widths. If the calibration-heater edge effects are taken into consideration during the passive mode calibration procedure, the new thermal exchange parameters yield experimental temperature profiles with smaller deviations from expectations and similar to those based on active mode calibration, as shown in Fig. S10 in the supplementary material.

There are situations when the active mode calibration method is more challenging to implement due to unknown substrates or the presence of additional films on the substrate which may also have unknown thermal properties or thicknesses. In these cases, the passive calibration method is more robust, as shown below. To exemplify these situations, SThM experiments were performed using 20-μm and 40-μm width heaters deposited on a 340-nm thin dielectric SiO_2 film on a silicon substrate. The tip-sample clearance was 300 nm. The experimental temperature profiles were determined using the measured average probe temperature rise for each location, the analytical model, and the passive mode thermal exchange parameters determined from Fig. 8(a). While all calibrations were performed on glass samples, the temperature profiles of test samples matched the theoretical predictions even when their substrate thermal conductivities varied by more than 100 times, as shown for heaters of different widths on silicon substrates in Fig. 11. Since silicon has a much larger thermal conductivity than glass,[35] the measured temperature rise profiles on silicon substrate are flatter than on glass substrate. The temperature rise profiles from Fig. 11 averaged over the physical extent of each heater are in good agreement (within between 2.9% and 3.5%) with the thermistor based average heater temperature rise reported in Table II.

Table II shows a comparison between average microheater temperatures, determined using thermistor based measurements, and averages calculated from SThM experimental temperature profiles from Figs. 9 to 11. Employing thermal exchange parameters from active calibration method gave the most accurate results, with microheater average temperature discrepancies smaller than 0.5%, except for situations when active calibration cannot be performed directly on the sample of interest. The passive calibration method yielded microheater average temperature discrepancies between 1.6% and 3.5% and was successfully employed even when sample thermal properties were unknown and active calibration cannot be performed. An example of using the passive calibration without the need for recalibration of the sample-probe thermal exchange parameters is given for microheaters deposited on a dielectric film on silicon substrate, when temperature measurement discrepancies are between 2.9% and 3.5%. However, forcing the thermal exchange parameters calibrated by the active method on glass substrates would give much large errors in this case, between 16.8% and 17.6% for 40-μm and 20-μm width heaters, respectively. This is because the probe-sample thermal exchange parameters determined by the active calibration method are dependent on the sample thermal conductivity.[10]

As 3DFEM results demonstrate (shown in the supplementary material), temperature profiles from similar heaters situated very close (2 μm) or away (40 μm) from each other can be accurately measured using the noncontact SThM technique and the analytical model developed in this work.

VI. SUMMARY AND CONCLUSIONS

A quantitative method to measure sample temperature profiles by SThM in noncontact mode was developed. In this technique, the thermal probe is scanned above the sample at a distance comparable with the mean free path of ambient gas molecules. A Three-Dimensional Finite Element Model (3DFEM) that includes the details of the heat transfer between the sample and the probe in the diffusive and transition heat conduction regimes was found to accurately simulate the temperature profiles measured using a Wollaston thermal probe setup. In order to simplify the data reduction for the local sample temperature, analytical models were developed for noncontact measurements using Wollaston probes. Two calibration strategies (active calibration and passive calibration) for the sample-probe thermal exchange parameters are presented. Both calibration methods use sample-probe thermal exchange resistance correlations developed using the 3DFEM to accurately capture effects due to sample-probe gap geometry and the thermal exchange radii in the diffusive and transition heat conduction regimes. The analytical data reduction methods were validated by experiments and 3DFEM simulations using microscale heaters deposited on glass and on dielectric films on silicon substrates. The deviation between the SThM determined and actual average microheater temperature rise was between 0.1% and 0.5% when using active calibration on samples with known thermal properties and between ~1.6% and 3.5% when using passive calibration, which is a more robust method that can be employed on samples with unknown thermal properties too. Therefore, the technique was validated irrespective of the samples' substrates and heater widths tested so far. Since thermal profiles collected at probe-sample clearances between 100 and 200 nm were not distinguishable, in this regime, the noncontact SThM method is insensitive to uncertainties due to the probe-sample clearance. This is due to a sample-probe thermal exchange resistance which is clearance independent in the transition regime. In conclusion, a robust noncontact SThM technique was developed which demonstrated accurate sample temperature measurements for probe-sample clearances in both transition and diffusive heat conduction regimes. The technique's principles demonstrated here with Wollaston probes and microscale heaters could be perhaps adapted to smaller diameter probes and demonstrated on samples with complex heating patterns.

SUPPLEMENTARY MATERIAL

See the supplementary material for microscopy images of the microheaters and SThM probe, a comparison between 3DFEM and analytical simulations of the thermal profiles of the SThM probe, an example of surface thermal profile around a microheater obtained from 3DFEM, the recalibration of the passive mode thermal exchange parameters and the beneficial effect on measured thermal profile accuracy after considering calibration-heater edge effects, 3DFEM based simulations showing accurate SThM near adjacent heaters with small and large distances between them, and discussions of the effects induced by variations in ambient heat transfer coefficient and ambient thermal conductivity.

NOMENCLATURE

A_p	cross-sectional area of the probe (m^2)
b	thermal exchange radius (m)
d	diameter of the probe (m)
D	tip-sample clearance at tip apex (m)
D_i	local tip-sample clearance (m)
E	electric field strength ($V\ m^{-1}$)
h_{eff}	effective heat transfer coefficient ($W\ m^{-2}\ K^{-1}$)
I	probe's current (A)
J	current density of the probe ($A\ m^{-2}$)
K	thermal conductivity of computational domains ($W\ m^{-1}\ k^{-1}$)
k_0	thermal conductivity of air in free space ($W\ m^{-1}\ K^{-1}$)
k_f	thermal conductivity of the air layer ($W\ m^{-1}\ K^{-1}$)
Kn	Knudsen number
k_p	thermal conductivity of the probe ($W\ m^{-1}\ K^{-1}$)
k_s	sample thermal conductivity ($W\ m^{-1}\ K^{-1}$)
L	half length of the probe (m)
Pr	Prandtl number
Q	volumetric heat source ($W\ m^{-3}$)
Q_s	heat transfer rate between probe tip and sample (W)
R	probe electrical resistance (Ω)
r	radius of the Wollaston wire probe (m)
R_C^{th}	thermal exchange resistance ($K\ W^{-1}$)
R_{p0}	no heating resistance (Ω)
R_S^{th}	sample thermal resistance ($K\ W^{-1}$)
T^*	probe local temperature rise above the ambient temperature (K)
T_{ave}^*	average probe temperature rise (K)
TCR_p	temperature coefficient of resistance of the probe (K^{-1})
$T_p{}^*$	probe tip temperature rise (K)
T_{ref}	ambient temperature value in simulation (K)
$T_s{}^*$	sample temperature rise (K)
$V_{photodetector}$	voltage signal across the photodetector (V)
V_{probe}	voltage signal across the probe (V)
V_R	voltage signal across series resistor of probe circuit (V)
V_{Rs}	voltage signal across series resistor of microheater circuit (V)
V_s	voltage signal across microheaters (V)

Greek letters

σ	electrical conductivity ($S\ m^{-1}$)
γ	ratio of the specific heats
Λ	mean free path of air in free space (m)
ρ_0	electrical resistivity of the probe (Ω m)
σ_T	thermal accommodation coefficient

Abbreviation

3DFEM	three-dimensional finite element model
AFM	atomic force microscopy
SThM	scanning thermal microscopy

REFERENCES

[1] R. Heiderhoff, A. Makris, and T. Riedl, "Thermal microscopy of electronic materials," Mater. Sci. Semicond. Process. **43**, 163 (2016).

[2] M. Kuball, S. Rajasingam, A. Sarua, M. Uren, T. Martin, B. T. Hughes, K. P. Hilton, and R. Balmer, "Measurement of temperature distribution in multi-finger AlGaN/GaN heterostructure field-effect transistors using micro-Raman spectroscopy," Appl. Phys. Lett. **82**, 124 (2003).

[3] A. Soudi, R. D. Dawson, and Y. Gu, "Quantitative heat dissipation characteristics in current-carrying GaN nanowires probed by combining scanning thermal microscopy and spatially resolved Raman spectroscopy," ACS Nano **5**, 255 (2011).

[4] K. E. Goodson and M. Asheghi, "Near-field optical thermometry," Microscale Thermophys. Eng. **1**, 225–235 (1997).

[5] T. Fujii, Y. Taguchi, T. Saiki, and Y. Nagasaka, "Near-field fluorescence thermometry using highly efficient triple-tapered near-field optical fiber probe," Rev. Sci. Instrum. **83**, 124901 (2012).

[6] D. Teyssieux, L. Thiery, and B. Cretin, "Near-infrared thermography using a charge-coupled device camera: Application to microsystems," Rev. Sci. Instrum. **78**, 034902 (2007).

[7] D. Teyssieux, D. Briand, J. Charnay, N. F. de Rooij, and B. Cretin, "Dynamic and static thermal study of micromachined heaters: The advantages of visible and near-infrared thermography compared to classical methods," J. Micromech. Microeng. **18**, 065005 (2008).

[8] A. Majumdar, "Scanning thermal microscopy," Annu. Rev. Mater. Sci. **29**, 505 (1999).

[9] E. Nasr Esfahani, F. Ma, S. Wang, Y. Ou, J. Yang, and J. Li, "Quantitative nanoscale mapping of three-phase thermal conductivities in filled skutterudites via scanning thermal microscopy," Natl. Sci. Rev. **5**, 59 (2017).

[10] A. Wilson and T. Borca-Tasciuc, "Quantifying non-contact tip-sample thermal exchange parameters for accurate scanning thermal microscopy with heated microprobes," Rev. Sci. Instrum. **88**, 074903 (2017).

[11] Y. Zhang, E. Castillo, R. Mehta, G. Ramanath, and T. Borca-Tasciuc, "A non-contact thermal microprobe for local thermal conductivity measurement," Rev. Sci. Instrum. **82**, 024902 (2011).

[12] A. A. Wilson, "Analysis of non-contact and contact probe-to-sample thermal exchange for quantitative measurements of thin film and nanostructure thermal conductivity by the scanning hot probe method," Ph.D. dissertation (Rensselaer Polytechnic Institute, Troy, New York, 2017).

[13] K. Kim, J. Chung, J. Won, O. Kwon, J. Sik Lee, S. Park, and Y. K. Choi, "Quantitative scanning thermal microscopy with double scan technique," Appl. Phys. Lett. **93**, 203115 (2008).

[14] W. Jeong, S. Hur, E. Meyhofer, and P. Reddy, "Scanning probe microscopy for thermal transport measurements," Nanoscale Microscale Thermophys. Eng. **19**, 279 (2015).

[15] J. Chung, K. Kim, G. Hwang, O. Kwon, S. Jung, J. Lee, J. W. Lee, and G. Tae Kim, "Quantitative temperature measurement of an electrically heated carbon nanotube using the null-point method," Rev. Sci. Instrum. **81**, 114901 (2010).

[16] J. Chung, K. Kim, G. Hwang, O. Kwon, Y. K. Choi, and J. S. Lee, "Quantitative temperature profiling through null-point scanning thermal microscopy," Int. J. Thermal Sci. **62**, 109 (2011).

[17] G. Hwang and O. Kwon, "Measuring the size dependence of thermal conductivity of suspended graphene disks using null-point scanning thermal microscopy," Nanoscale **8**, 5280 (2016).

[18] F. Menges, H. Riel, A. Stemmer, and B. Gotsmann, "Temperature mapping of operating nanoscale devices by scanning probe thermometry," Nat. Commun. **7**, 10874 (2016).

[19] F. Menges, F. Könemann, H. Schmid, P. Mensch, M. Dittberner, S. Karg, H. Riel, and B. Gotsmann, "Local thermometry of self-heated nanoscale devices," in *Proceedings of 2016 IEEE International Electron Devices Meeting (IEDM)* (IEEE, 2016), pp. 3–7.

[20] F. Menges, H. Riel, A. Stemmer, and B. Gotsmann, "Quantitative thermometry of nanoscale hot spots," Nano Lett. **12**, 596 (2012).

[21] T. Borca-Tasciuc, "Scanning probe methods for thermal and thermoelectric property measurements," Annu. Rev. Heat Transfer **16**, 211 (2013).

[22] H. Fischer, "Quantitative determination of heat conductivities by scanning thermal microscopy," Thermochim. Acta **425**, 69 (2005).

[23] P. Klapetek, I. Ohlídal, and J. Buršík, "Applications of scanning thermal microscopy in the analysis of the geometry of patterned structures," Surf. Interface Anal. **38**, 383 (2006).

[24] S. Gomès, A. Assy, and P.-O. Chapuis, "Scanning thermal microscopy: A review," Phys. Status Solidi A **212**, 477 (2015).

[25] W. Jeong, K. Kim, Y. Kim, W. Lee, and P. Reddy, "Corrigendum: Characterization of nanoscale temperature fields during electromigration of nanowires," Sci. Rep. **4**, 5690 (2014).

[26] K. Kim, W. Jeong, W. Lee, and P. Reddy, "Ultra-high vacuum scanning thermal microscopy for nanometer resolution quantitative thermometry," ACS Nano **6**, 4248 (2012).

[27] Y.-J. Yu, M. Y. Han, S. Berciaud, A. B. Georgescu, T. Heinz, L. E. Brus, K. Kim, and P. Kim, "High-resolution spatial mapping of the temperature distribution of a Joule self-heated graphene nanoribbon," Appl. Phys. Lett. **99**, 183105 (2011).

[28] L. Shi, J. Zhou, P. Kim, A. Bachtold, A. Majumdar, and P. McEuen, "Thermal probing of energy dissipation in current-carrying carbon nanotubes," J. Appl. Phys. **105**, 104306 (2009).

[29] P.-O. Chapuis, J.-J. Greffet, K. Joulain, and S. Volz, "Heat transfer between a nano-tip and a surface," Nanotechnology **17**, 2978 (2006).

[30] Y. Zhang, W. Zhu, F. Hue, M. Lanza, T. Borca-Tasciuc, and M. M. Rojo, "A review on principles and applications of scanning thermal microscopy (SThM)—A review," Adv. Funct. Mater. 1900892 (2019).

[31] K. Kim, L. Cui, and V. Fernández-Hurtado, "Radiative heat transfer in the extreme near field," Nature **528**, 387 (2015).

[32] L. Han, "Development of a non-contact scanning temperature sensing method and characterization of ZT in pnictogen-chalcogen alloys," Ph.D. dissertation (Rensselaer Polytechnic Institute, Troy, New York, 2014).

[33] A. Wilson, M. Rojo, B. Abad, J. Perez Taborda, J. Maiz, J. Schomacker, M. Martín-González, D.-A. Borca-Tasciuc, and T. Borca-Tasciuc, "Thermal conductivity measurements of high and low thermal conductivity films using a scanning hot probe method in the 3ω mode and novel calibration strategies," Nanoscale **7**, 15404 (2015).

[34] COMSOL Multiphysics, COMSOL multiphysics user guide (Version 4.3 a), 2012.

[35] R. H. Perry and D. W. Green, *Perry's Chemical Engineers' Handbook*, 7th ed. (McGraw-Hill, 1997).

[36] J. Bodzenta, J. Juszczyk, and M. Chirtoc, "Quantitative scanning thermal microscopy based on determination of thermal probe dynamic resistance," Rev. Sci. Instrum. **84**, 093702 (2013).

[37] M. Calvert and J. Baker, "Thermal conductivity and gaseous microscale transport," J. Thermophys. Heat Transfer **12**, 138 (1998).

[38] W. D. Zhou, B. Liu, S. yu, and W. Hua, "Rarefied-gas heat transfer in micro- and nanoscale Couette flows," Phys. Rev. E **81**, 011204 (2010).

[39] C.-Y. Zhu, Z.-Y. Li, and W.-Q. Tao, "Theoretical and DSMC studies on heat conduction of argon gas in a cubic nanopore," J. Heat Transfer **139**, 052405 (2017).

[40] Y. Zhang, "Thermal and thermoelectric transport in nanostructured materials from pnictogen chalcogenide nanoplate crystals," Ph.D. dissertation (Rensselaer Polytechnic Institute, Troy, New York, 2011).

[41] Y. Ge, Y. Zhang, J. Booth, J. M. R. Weaver, and P. S. Dobson, "Quantification of probe-sample interactions of a scanning thermal microscope using a nanofabricated calibration sample having programmable size," Nanotechnology **27**, 325503 (2016).